Spin-polarized saddle points in the topological surface states of elemental bismuth revealed by pump-probe spin- and angle-resolved photoemission spectroscopy

Yuto Fukushima,[1] Kaishu Kawaguchi,[1] Kenta Kuroda ●,[2,3,4] Masayuki Ochi ●,[5,6] Motoaki Hirayama,[7,8] Ryo Mori ●,[1]
Hiroaki Tanaka ●,[1] Ayumi Harasawa ●,[1] Takushi Iimori,[1] Zhigang Zhao,[1,9] Shuntaro Tani ●,[1] Koichiro Yaji ●,[10] Shik Shin,[11]
Fumio Komori ●,[1] Yohei Kobayashi ●,[1] and Takeshi Kondo ●[1,12,*]

[1]*Institute for Solid State Physics, The University of Tokyo, Kashiwa, Chiba 277-8581, Japan*
[2]*Graduate School of Advanced Science and Engineering, Hiroshima University, Higashi-hiroshima, Hiroshima 739-8526, Japan*
[3]*International Institute for Sustainability with Knotted Chiral Meta Matter (WPI-SKCM², Hiroshima University,*
Higashi-hiroshima, Hiroshima 739-8526, Japan
[4]*Research Institute for Semiconductor Engineering, Hiroshima University, Higashi-Hiroshima, Hiroshima 739-8527, Japan*
[5]*Department of Physics, Osaka University, Toyonaka, Osaka 560-0043, Japan*
[6]*Forefront Research Center, Osaka University, Toyonaka, Osaka 560-0043, Japan*
[7]*Department of Applied Physics, University of Tokyo, Tokyo 113-8656, Japan*
[8]*RIKEN Center for Emergent Matter Science (CEMS), Wako, Saitama 351-0198, Japan*
[9]*School of Information Science and Engineering, Shandong University, Qingdao, 266237, China*
[10]*Center for Basic Research on Materials, National Institute for Materials Science (NIMS), Tsukuba, Ibaraki 305-0003, Japan*
[11]*Office of University Professor, The University of Tokyo, Kashiwa, Chiba 277-8581 Japan*
[12]*Trans-scale Quantum Science Institute, The University of Tokyo, Tokyo 113-0033, Japan*

We use pump-probe, spin- and angle-resolved photoemission spectroscopy (ARPES) with a 10.7 eV laser accessible up to the Brillouin zone edge, and reveal the entire band structure around the Fermi level, including the unoccupied side, for the elemental bismuth (Bi) with the spin-polarized surface states. Our data identify Bi as in a strong topological insulator phase ($Z_2 = 1$) against the prediction of most band calculations. We unveil that the unoccupied topological surface states possess spin-polarized saddle points yielding the van Hove singularity. The unique feature provides an excellent platform for the future development of optospintronics.

Elemental bismuth has the largest spin-orbit interaction among all the stable and safe elements, making it a popular choice for generating spin currents in spintronics research [1–5]. The interest in spin currents has grown significantly following the discovery of the spin Hall effect [6–9] and the Edelstein effect [10–12], which are brought by the occupied states in matters with strong spin-orbital interaction. Recently, a new generation of spintronics, so-called optospintronics [13–18], has been actively investigated. Unlike traditional spintronics, optospintronics actively exploit the unoccupied side of a material's band structure through photoexcitation, potentially revealing unexplored material functionalities. Despite their potential significance, the spin-polarized band structures on the unoccupied side of materials remain elusive due to the difficulties associated with their direct observation. Elemental bismuth, with its largely spin-split surface bands [19,20], emerges as one of the most promising materials for optospintronics research. However, its critical unoccupied side has been awaiting experimental observation.

The elemental bismuth (Bi) is also the most popular element for a material design realizing topological phases of matter. Note that prototype Z_2 topological insulators (TIs) all contain the element: prototype strong TIs were realized in Bi_2Se_3 and Bi_2Te_3 [21–23], and weak TIs were in β-Bi_4I_4 [24–26] and $Bi_{14}Rh_3I_9$ [27–29]. Surprisingly, however, the bulk topology of the elemental Bi itself has not yet been identified and continues to be debated [30–36], even though its properties, including spin-polarized surface states, have been vigorously investigated for so many years [19,20,37–40]. Recently, a possible higher-order topological state has been suggested for the bulk Bi by extending the topological classification to Z_4 [41,42], accumulating huge attention. However, this is on the basis that Bi is topologically trivial ($Z_2 = 0$) within the Z_2 index. The bulk topology of the elemental Bi is, therefore, not only a longstanding issue but also, right now one of the central topics in condensed matter physics.

The bulk topology of Bi can be experimentally determined by identifying how two surface bands (SS1 and SS2) are connected into the bulk conduction and valence bands (BCB and BVB) around $\overline{M}$, as represented in Fig. 1. Despite these simple criteria, there are several reasons for this issue remaining controversial.

(1) High-quality Bi is commonly prepared as films. Bi films get free standing around 15 BLs (6 nm) [43], and stress from a substrate is totally removed when thicker than ∼25 BLs (∼10 nm) [44]. However, an interaction between the front and back surface states even in relatively thick films

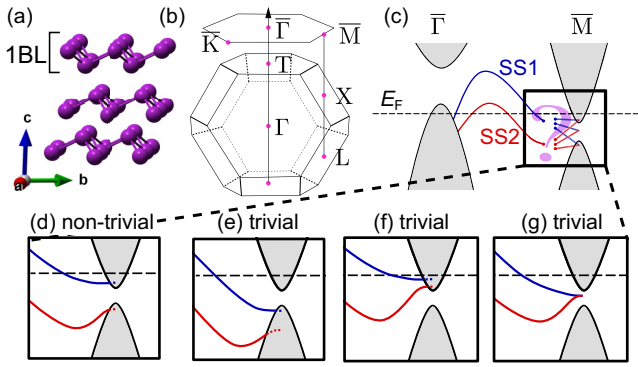*Contact author: kondo1215@issp.u-tokyo.ac.jp

FIG. 1. (a) Crystal structure of Bi in the (111) orientation. (b) Brillouin zone for bulk and (111) surface. (c) Schematic band structure along the $\overline{\Gamma}$ - $\overline{M}$ direction on the Bi(111) surface. Blue and red lines show the surface bands (SS1 and SS2) with in-plane spin polarization in opposite directions. (d)–(g) All possible relationships between surface and bulk bands around $\overline{M}$ corresponding to different bulk topologies. [31].

as 200 BLs may open a gap in the surface states and mislead the bulk topology [33,35,45].

(2) The entire band structure should be determined by experiments for a fair comparison with band calculations. However, this cannot be accomplished by a standard ARPES observing only the occupied states. One way of visualizing the unoccupied band is to raise the sample temperature and detect thermally excited electronic states above the Fermi level (E_F). However, the original bulk topology might be altered by lattice expansion inevitable at high temperatures [46,47].

(3) The bulk band gap around $\overline{M}$ is so small ($\sim$15 meV), making it hard to clarify the connections of surface bands to the bulk bands [48,49].

In this Letter, we overcome all these difficulties and clarify the genuine topological state in the elemental Bi. Following are our solutions (s1)–(s3) to (1)–(3).

(s1) We prepare a film of $\sim$1000 BLs ($\sim$0.4 μm), which is, according to theory [35], thick enough to make the overlap of wavefunction between the front and back surface states negligible.

(s2) We use a pump-probe spin-ARPES we recently developed [50], and unveil the band structure including the unoccupied states near the Fermi level over the entire Brillouin zone (BZ). Importantly, this technique allows observing unoccupied states without raising the lattice temperature by taking data just after pumping.

(s3) We employ spin-resolved spectra, which can distinguish between the surface and bulk bands with and without the spin polarization, respectively, to identify whether each of the two surface bands is connected to the conduction band or the valence band.

These experiments conclusively identify the bulk band topology of the elemental Bi to be nontrivial ($Z_2 = 1$). Our state-of-the-art pump-probed spin-ARPES [50] further reveals a unique feature in the unoccupied surface band: spin-polarized saddle points that form a hexagonal helical spin texture and generate the van Hove singularity (vHS) in the density of states. This could be an iconic structure for the

future optospintronics application with Bi, which controls the spin current by photoexcitation [16,51–54].

Single-crystal Bi(111) films of $\sim$1000 BL ($\sim$0.4 μm) were prepared *in situ* by depositing Bi on a Si(111) 7 × 7 surface (see more details in the Supplemental Material [55]). All ARPES measurements were performed with a 10.7 eV laser generated by a home-built Yb: fiber pulse laser [56,57]. The fundamental Yb: fiber laser (1.19 eV) was also used as a pump light. The energy resolution was $\sim$20 meV and $\sim$25 meV for pump-probe ARPES and pump-probe spin-SARPES, respectively. The time resolution was 360 fs. We used a mild pump (0.08 mJ/cm^2) preventing a lattice vibration. The high repetition rate of the laser (1MHz) and a high-efficiency spin-detector (VLEED) enabled us to obtain a sufficient count rate of spin signals. All experiments were performed around 70 K using *p*-polarized light for both the pump and probe. Details about our newly developed ARPES system are discussed elsewhere [50].

First, we investigate the spin-integrated band structure of Bi(111). Figures 2(a) and 2(b) plot the Fermi surface map and the occupied band dispersion along $\overline{\Gamma}$-$\overline{M}$ measured without pumping. We confirm well-known surface bands: a hexagonal electron pocket around $\overline{\Gamma}$, petal-like hole pockets surrounding it, and an elongated electron pocket around $\overline{M}$ [19,20]. These are formed by two surface bands (SS1 and SS2) connecting to bulk bands around $\overline{\Gamma}$ and $\overline{M}$. We further perform the pump-probe measurements and successfully visualize the bands up to the unoccupied side [Fig. 2(c)], including the bulk conduction band (BCB) at $\overline{\Gamma}$.

Figure 2(d) displays the contour energy maps at different binding energies on the unoccupied side. Interestingly, we find that separated hexagonal and petal-like pockets observed at lower energy (see $E - E_F = 0.15$ eV) get closer together with increasing energy and touch with each other at around 0.2 eV. Eventually, these two separated pockets turn to continuous parallel segments of enlarged energy contours at $E - E_F = 0.25$ eV (see the regions of dotted light blue rectangles). To understand the detailed band structure around this momentum region, we exhibit the energy dispersions along two momentum cuts [marked by magenta lines of **e** and **f** in Fig. 2(d)] in Figs. 2(e) and 2(f), respectively. We find that the cut along k_x [line **e** in Fig. 2(d)] shows that the touching point [arrow in Fig. 2(e)] is located at the top of the upward energy dispersion, while the cut along k_y [line **f** in Fig. 2(d)] shows it [arrow in Fig. 2(f)] to be located at the bottom of the downward energy dispersion. Therefore, this energy state is a saddle point, which forms the van Hove singularity in the density of states [58,59]. It is further demonstrated in Fig. 2(g) by three-dimensionally plotting the ARPES data along the k_x, k_y, and energy. The same saddle point is placed at six locations in the surface BZ [Fig. 2(f)], which forms a helical spin structure, as revealed below.

The spin polarization is investigated by pump-probe spin-ARPES. Figure 3(b) plots the in-plane Y component of spin polarization (S_Y) for the orange rectangular region in Fig. 2(a). Thanks to the pump-probe technique, the spin-polarized states of surface bands (SS1 and SS2) are unveiled not only on the occupied side but also on the unoccupied side. Notably, the sign reversal of spin between SS1 and SS2 is clearly exhibited. Importantly, our experiments demonstrate that the saddle
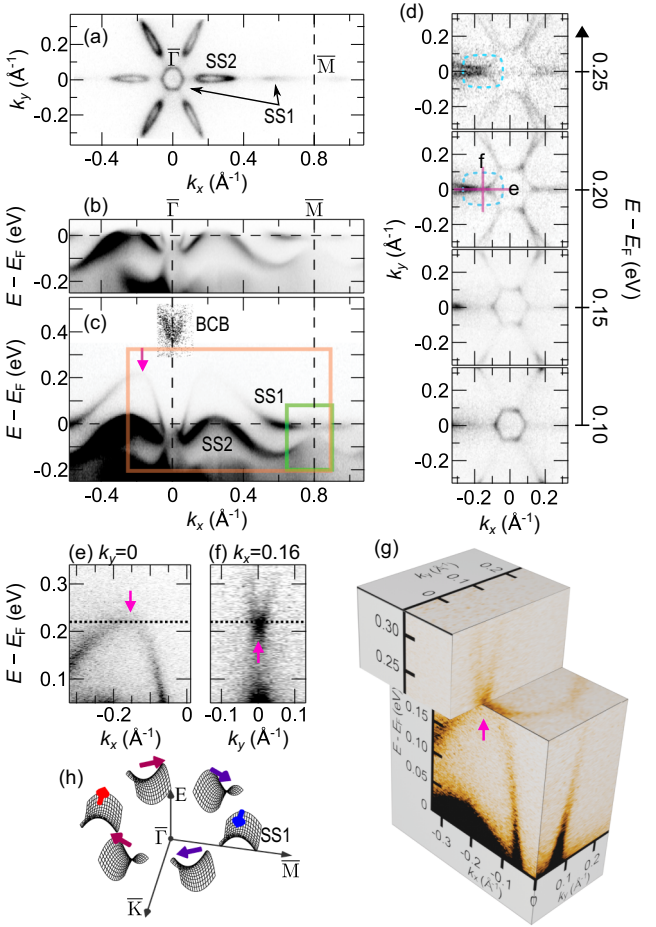
FIG. 2. Band structures of Bi revealed by pump-probe ARPES. (a) Fermi surface map. (b), (c) Band dispersion along $\overline{\Gamma}$ - $\overline{M}$ measured without and with pump. (d) Energy contour maps on the unoccupied side from 0.10 to 0.25 eV. (e), (f) Band dispersions crossing the saddle point along k_x and k_y [momentum cuts **e** and **f** marked in (d)]. (g) Three-dimensionally plotted ARPES intensities along k_x, k_y, and energy. (h) Schematic of spin-polarized saddle points with a hexagonal structure. Magenta arrows in (c), (e), (f), and (g) indicate the saddle point.
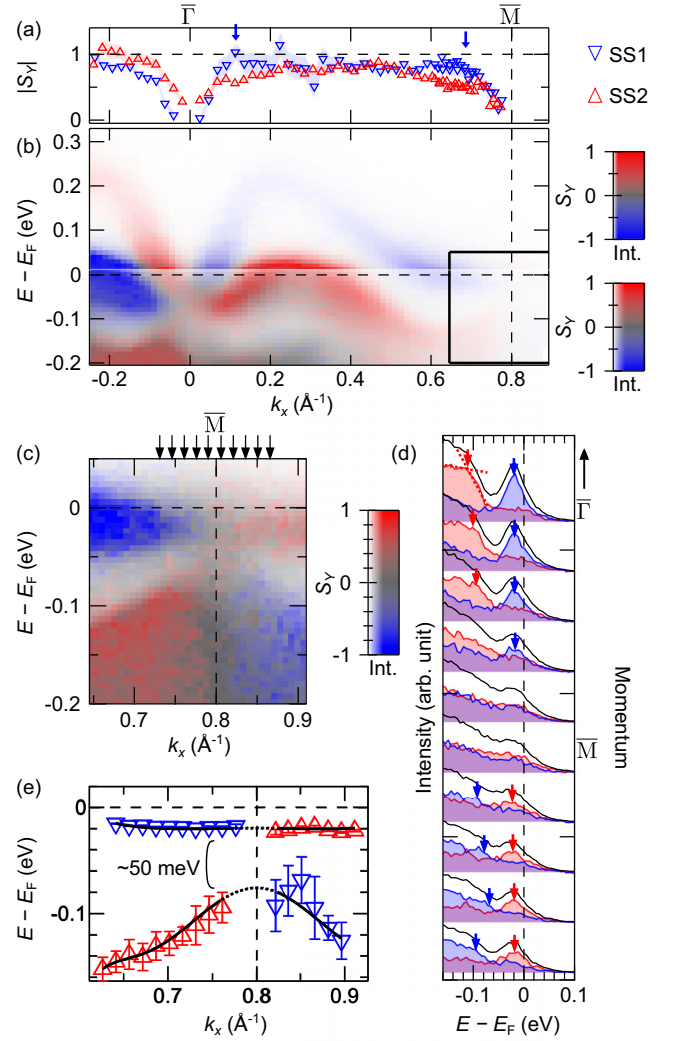

FIG. 3. Spin texture of surface states in Bi revealed by pump-probe spin-ARPES. (a), (b) Spin polarization and spin-polarized band along $\overline{\Gamma}$ - $\overline{M}$, respectively. Red and blue represent up and down spin in the Y direction for two surface bands (SS1 and SS2). The painted areas in (a) represent errors (see more details in the Supplemental Material [55]). (c) High-resolution map of spin polarization around $\overline{M}$ within the black frame in (b). (d) Spin-resolved EDCs at k's marked by arrows in (c). Energy positions of surface bands are pointed by red and blue arrows. Black curves are the addition of the up- and down-spin spectra. (e) Surface bands determined from spin-resolved EDCs. Fitting curves to the data (solid and dotted lines) are overlaid.

points yielding the vHS around 0.2 eV are spin polarized with a helical spin structure, as illustrated in Fig. 2(f).

We estimate $|S_Y|$ for the upper and lower surface bands along $\overline{\Gamma}$ - $\overline{M}$ in Fig. 3(a) to examine how the spin-polarized surface states are mixed with or absorbed into the bulk states without spin polarization. The 100% spin polarization should be observed for the surface states if the following two conditions are fulfilled [60]. One is that the E-k points are far from the time-reversal invariant momenta ($\overline{\Gamma}$ and $\overline{M}$), at which the up and down spin are inevitably degenerate. Second is that they are free from hybridization with the bulk states which reduces spin polarization. As expected, while S_Y's of SS1 and SS2 are close to 100% in the momentum range far from $\overline{\Gamma}$ and $\overline{M}$ (0.2 Å^{-1} < k_x < 0.6 Å^{-1}), these decrease and eventually become almost zero at $\overline{\Gamma}$ and $\overline{M}$. Nevertheless, we find a clear difference between $S_Y(k_x)$'s of the upper and lower surface bands: the latter decreases more rapidly than the former with approaching $\overline{\Gamma}$ and $\overline{M}$ where the valence bands are situated,

as represented by blue arrows in Fig. 3(a). This indicates that the lower surface band is absorbed to (or hybridized with) the bulk bands extensively around $\overline{\Gamma}$ and $\overline{M}$. Note that the other spin components, S_X and S_Z, are zero [60] due to the mirror operation M_x changing the spin direction as $S_X \rightarrow -S_X$, $S_Y \rightarrow S_Y$, $S_Z \rightarrow -S_Z$ [61].

Since the spin-polarization signals originate from the surface states, the surface bands can be determined separately from the bulk states by tracing the peak positions of the spin-polarized spectra. In particular, we measured the spin-polarization map with high precision for the bands around $\overline{M}$

[Fig. 3(c)], which is the key momentum region to determining the bulk topology of Bi. Figure 3(d) plots spin-resolved energy distribution curves (EDCs) at k's marked by arrows in Fig. 3(c). The spin-integrated EDCs (black lines) are also superposed. Although peaks are observed for the upper surface band slightly below E_F, only a hump structure, poorly defined as a quasiparticle, is obtained for the lower surface band around -0.1 eV. This agrees with our assertion that the lower surface band is significantly hybridized with the bulk valence band around $\overline{M}$ with a broad spectral continuum; the bulk state is observed as a continuum projected onto the surface due to the k_z broadening typical for ARPES, which is a surface-sensitive technique.

The spectral hump has a shoulder structure as a remnant of the surface band. The lower surface band is determined by tracing their energies, obtained as the crossing point of two lines fitted to a spectrum, as demonstrated in Fig. 3(d). In Fig. 3(e), we plot the results together with the upper surface band. In both bands, plots are missing close to $\overline{M}$, where the spin-polarization is zero; those are, instead, estimated by extrapolating a curve fitted to the data (dotted curves). The upper surface band is almost flat, whereas the lower surface band disperses upward. However, they stay off each other, opening a band gap of ~ 50 meV at $\overline{M}$. These observations eliminate the case of Fig. 1(g) predicted by most band calculations [34,35].

To pin down the relationship between the surface and bulk bands further, we measure high statistics data of pump-probe ARPES around $\overline{M}$ [Fig. 4(a)]. The obtained intensity map [Fig. 4(a)] shows a parabola-shaped spectral continuum for the bulk valence and conduction bands (BVB and BCB), other than strong intensities for the surface bands with sharp spectral peaks. To examine the bulk states in more detail, we plot momentum distribution curves (MDCs) around the bulk band gap in Fig. 4(b), where the intensities for the bulk signals are painted by colors (green and orange for BCB and BVB, respectively). Their intensities reduce the momentum width by approaching each other and eventually disappear without merging together. This indicates that a gap (<0.02 eV) much smaller than that of the surface bands (~ 0.05 eV) opens around $E - E_F = -0.025$ eV. The value of the bulk band gap we observed is consistent with those ($11 \sim 15$ meV) that have been determined by electromagnetic experiments over the past half-century [48,49,62–64]. The bulk states are expressed in Fig. 4(c) with color bars. In the same panel, we overlay the upper and lower surface bands (dashed lines) determined from spin-polarized spectra in Fig. 3(e). The result shows that a small portion of the upper surface is absorbed into the bottom of BCB, whereas a large portion of the lower surface band is into BCB around $\overline{M}$, as depicted in Fig. 4(d). The relation between surface and bulk bands corresponds to the case of Fig. 1(a). Hence, the bulk topology of the elemental Bi is nontrivial ($Z_2 = 1$; strong topological insulator phase), against most theoretical predictions [34,35] except for some exceptions [36].

In previous studies, the comparison between experiments and calculations on the bands of Bi has been limited to the occupied states [37,65]. In addition, a standard ARPES is out of reach for decisively distinguishing surface and bulk bands. These factors have prevented one from fairly evaluating the
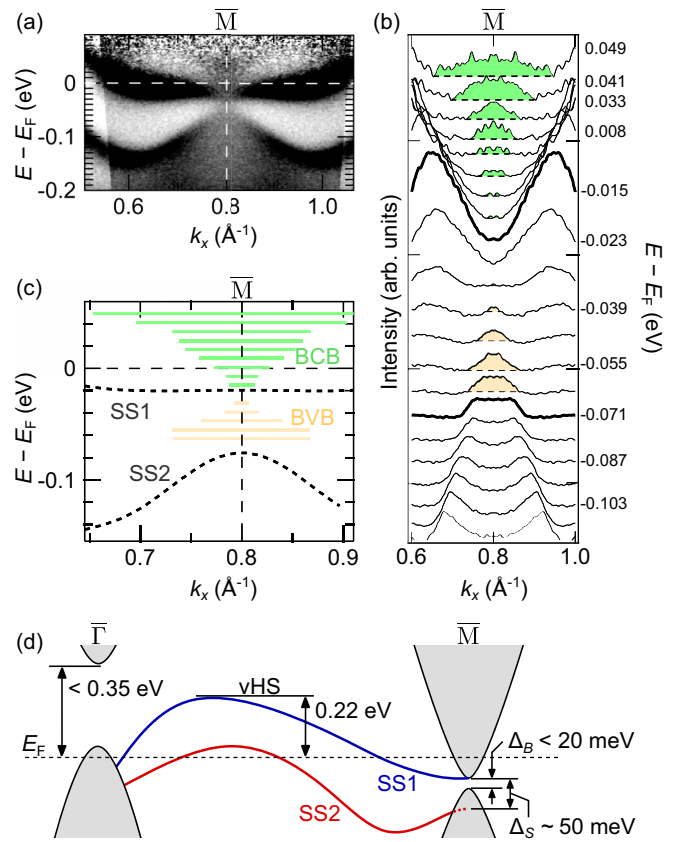

FIG. 4. Bulk bands and their relationship with surface bands. (a) Pump-probe ARPES map around $\overline{M}$. Here, the original spectra are symmetrized across $\overline{M}$ to remove the matrix element effect. They are also divided by the Fermi-Dirac distribution function at the electron temperature (250 K) estimated from the spectral edge broadening due to the pumping. (b) MDCs of (a). Thick black lines represent energies of two surface bands. Intensities of BCB and BVB are each painted green and orange. (c) Bulk bands (color bars) obtained from (b) and surface bands (dashed lines) determined in Fig. 3(e) are superimposed. (d) Schematic band structure and characteristic energies obtained in our experiments.

reliability of band calculations for the elemental Bi. Among modern experimental techniques, a pump-probe spin-ARPES is the only means allowing a full comparison between the experiments and calculations, and it was first employed for Bi in this work.

The characteristic values of the unoccupied bands we obtained using this experimental technique are described in Fig. 4(d). In the table of Fig. 5(a), we compare our results with previous theoretical studies with different calculation methods, generalized gradient approximation (GGA), and quasiparticle self-consistent GW (QSGW) [34,35], both expecting the bulk topology to be trivial ($Z_2 = 0$). The GGA calculations show good agreement with the experiments for the energies of BCB bottoms and vHS; however, the bulk band gap at $\overline{M}$, $\Delta_B(\overline{M})$, is over estimated by ~ 0.1 eV. In contrast, $\Delta_B(\overline{M})$ shows good agreement in the QSGW calculations, in which, however, the bottom energy of BCB at $\overline{\Gamma}$ and the energy of vHS have large discrepancies by about 0.15 eV. We also conducted calculations with the modified Becke-Johnson
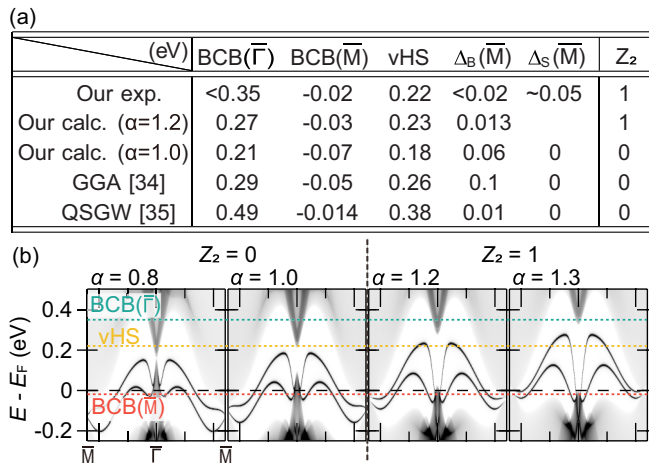
(a)

(eV)	BCB($\overline{\Gamma}$)	BCB($\overline{M}$)	vHS	Δ_B($\overline{M}$)	Δ_S($\overline{M}$)	Z_2
Our exp.	<0.35	-0.02	0.22	<0.02	~0.05	1
Our calc. (α=1.2)	0.27	-0.03	0.23	0.013		1
Our calc. (α=1.0)	0.21	-0.07	0.18	0.06	0	0
GGA [34]	0.29	-0.05	0.26	0.1	0	0
QSGW [35]	0.49	-0.014	0.38	0.01	0	0

(b)

FIG. 5. (a) Comparison of characteristic energies in band structures obtained: bottoms of BCB at $\overline{\Gamma}$ and $\overline{M}$, energy of vHS, and energy gaps at $\overline{M}$ between BCB and BVB (Δ_B) and between SS1 and SS2 (Δ_S). Bulk topology is also listed. α is a parameter of the modified Becke-Johnson potential used in our calculations. (b) First-principles band calculations of semi-infinite layer Bi(111) along $\overline{\Gamma}$-$\overline{M}$ for different α values. α=1.0 corresponds to the original band, whereas the states with α less than 1.0 are assigned as trivial ($Z_2 = 0$), and those with larger αs are as nontrivial ($Z_2 = 1$).

potential (see details in the Supplemental Material [55]), and listed the obtained parameters in the table of Fig. 5(a). Again, a mismatch with experiments by more than 0.1 eV is inevitable in the original result (α=1.0); however, we find that tuning the parameter α can make the calculations match our data. As demonstrated in Fig. 5(b), overall band positions

in experiments are reproduced around α=1.2 relatively well. The bulk topology of this calculation is a strong TI state ($Z_2 = 1$), supporting our conclusion.

In conclusion, we revealed the entire band structure of Bi around the Fermi level including the unoccupied side for the first time, which became available owing to our recent development of a pump-probe spin-ARPES. These data unveiled two key features. One is that Bi is in the strong topological insulator phase ($Z_2 = 1$), which was obtained by solving all the previous difficulties. The spin-split surface bands are, therefore, not due to the trivial Rashba state but to the topological state. This result disagrees with the prediction that Bi is a trivial semimetal or a higher-order topological insulator; see more detailed arguments in the Supplemental Material [55]. Second, we unveiled that the topologically protected surface bands possess the spin-polarized saddle points yielding van Hove singularity in the unoccupied density of states. Interestingly, they form a spin helical structure, indicating the availability of controlling massive spin currents by direct excitation with circularly polarized light. The pinpoint tunability of the spin current generation with specific light is a major advantage of utilizing unoccupied states of matter. Following this concept, the elemental Bi with a topological nature provides an excellent platform for developing optospintronics expected as future technology.

[1] Y. Fuseya, M. Ogata, and H. Fukuyama, Spin-Hall effect and diamagnetism of dirac electrons, J. Phys. Soc. Jpn. **81**, 093704 (2012).

[2] D. Hou, Z. Qiu, K. Harii, Y. Kajiwara, K. Uchida, Y. Fujikawa, H. Nakayama, T. Yoshino, T. An, K. Ando, Xiaofeng Jin, and E. Saitoh, Interface induced inverse spin Hall effect in bismuth/permalloy bilayer, Appl. Phys. Lett. **101**, 042403 (2012).

[3] H. Emoto, Y. Ando, E. Shikoh, Y. Fuseya, T. Shinjo, and M. Shiraishi, Conversion of pure spin current to charge current in amorphous bismuth, J. Appl. Phys. **115**, 17C507 (2014).

[4] H. Emoto, Y. Ando, G. Eguchi, R. Ohshima, E. Shikoh, Y. Fuseya, T. Shinjo, and M. Shiraishi, Transport and spin conversion of multicarriers in semimetal bismuth, Phys. Rev. B **93**, 174428 (2016).

[5] D. Yue, W. Lin, J. Li, X. Jin, and C. L. Chien, Spin-to-charge conversion in Bi films and BiAg bilayers, Phys. Rev. Lett. **121**, 037201 (2018).

[6] M. I. Dyakonov, Possibility of orienting electron spins with current, JETP Lett. USSR **13**, 467 (1971).

[7] J. E. Hirsch, Spin Hall effect, Phys. Rev. Lett. **83**, 1834 (1999).

[8] Y. K. Kato, R. C. Myers, A. C. Gossard, and D. D. Awschalom, Observation of the spin Hall effect in semiconductors, Science **306**, 1910 (2004).

[9] J. Wunderlich, B. Kaestner, J. Sinova, and T. Jungwirth, Experimental observation of the spin-Hall effect in a two-dimensional spin-orbit coupled semiconductor system, Phys. Rev. Lett. **94**, 047204 (2005).

[10] V. Edelstein, Spin polarization of conduction electrons induced by electric current in two-dimensional asymmetric electron systems, Solid State Commun. **73**, 233 (1990).

[11] Y. K. Kato, R. C. Myers, A. C. Gossard, and D. D. Awschalom, Current-induced spin polarization in strained semiconductors, Phys. Rev. Lett. **93**, 176601 (2004).

[12] J. C. R. Sánchez, L. Vila, G. Desfonds, S. Gambarelli, J. P. Attané, J. M. De Teresa, C. Magén, and A. Fert, Spin-to-charge conversion using Rashba coupling at the interface between non-magnetic materials, Nat. Commun. **4**, 2944 (2013).

[13] S. Sangiao, J. M. De Teresa, L. Morellon, I. Lucas, M. C. Martinez-Velarte, and M. Viret, Control of the spin to charge conversion using the inverse Rashba-Edelstein effect, Appl. Phys. Lett. **106**, 172403 (2015).

[14] G. Yumoto, F. Sekiguchi, R. Hashimoto, T. Nakamura, A. Wakamiya, and Y. Kanemitsu, Rapidly expanding spin-polarized exciton halo in a two-dimensional halide perovskite at room temperature, Sci. Adv. **8**, eabp8135 (2022).

[15] A. V. Kimel, A. Kirilyuk, F. Hansteen, R. V. Pisarev, and T. Rasing, Nonthermal optical control of magnetism and ultrafast

laser-induced spin dynamics in solids, J. Phys.: Condens. Matter **19**, 043201 (2007).

[16] H. Hirose, N. Ito, M. Kawaguchi, Y.-C. Lau, and M. Hayashi, Circular photogalvanic effect in Cu/Bi bilayers, Appl. Phys. Lett. **113**, 222404 (2018).

[17] S. Aftab, H. H. Hegazy, and M. Z. Iqbal, Recent advances in 2D TMD circular photo-galvanic effects, Nanoscale **15**, 3651 (2023).

[18] K. Kuroda, J. Reimann, K. A. Kokh, O. E. Tereshchenko, A. Kimura, J. Güdde, and U. Höfer, Ultrafast energy- and momentum-resolved surface Dirac photocurrents in the topological insulator, Phys. Rev. B **95**, 081103 (2017).

[19] C. R. Ast and H. Höchst, Fermi surface of Bi (111) measured by photoemission spectroscopy, Phys. Rev. Lett. **87**, 177602 (2001).

[20] Y. M. Koroteev, G. Bihlmayer, J. Gayone, E. V. Chulkov, S. Blügel, P. M. Echenique, and P. Hofmann, Strong spin-orbit splitting on Bi surfaces, Phys. Rev. Lett. **93**, 046403 (2004).

[21] H. Zhang, C.-X. Liu, X.-L. Qi, X. Dai, Z. Fang, and S.-C. Zhang, Topological insulators in Bi_2Se_3, Bi_2Te_3 and Sb_2Te_3 with a single Dirac cone on the surface, Nat. Phys. **5**, 438 (2009).

[22] Y. Xia *et al.*, Observation of a large-gap topological-insulator class with a single Dirac cone on the surface, Nat. Phys. **5**, 398 (2009).

[23] Y. L. Chen *et al.*, Experimental realization of a three-dimensional topological insulator, Bi_2Te_3, Science **325**, 178 (2009).

[24] C.-C. Liu, J.-J. Zhou, Y. Yao, and F. Zhang, Weak topological insulators and composite Weyl semimetals: β-Bi_4X_4 ($X =$ Br, I), Phys. Rev. Lett. **116**, 066801 (2016).

[25] G. Autès *et al.*, A novel quasi-one-dimensional topological insulator in bismuth iodide β-Bi_4I_4, Nat. Mater. **15**, 154 (2016).

[26] R. Noguchi *et al.*, A weak topological insulator state in quasi-one-dimensional bismuth iodide, Nature (London) **566**, 518 (2019).

[27] B. Rasche, A. Isaeva, M. Ruck, S. Borisenko, V. Zabolotnyy, B. Büchner, K. Koepernik, C. Ortix, M. Richter, and J. van den Brink, Stacked topological insulator built from bismuth-based graphene sheet analogues, Nat. Mater. **12**, 422 (2013).

[28] B. Rasche, A. Isaeva, A. Gerisch, M. Kaiser, W. Van den Broek, C. T. Koch, U. Kaiser, and M. Ruck, Crystal growth and real structure effects of the first weak 3D stacked topological insulator $Bi_{14}Rh_3I_9$, Chem. Mater. **25**, 2359 (2013).

[29] C. Pauly *et al.*, Subnanometre-wide electron channels protected by topology, Nat. Phys. **11**, 338 (2015).

[30] Y. Ohtsubo, L. Perfetti, M. O. Goerbig, P. L. Fèvre, F. Bertran, and A. Taleb-Ibrahimi, Non-trivial surface-band dispersion on Bi(111), New J. Phys. **15**, 033041 (2013).

[31] S. Ito *et al.*, Proving nontrivial topology of pure bismuth by quantum confinement, Phys. Rev. Lett. **117**, 236402 (2016).

[32] Y. Ohtsubo and S.-I. Kimura, Topological phase transition of single-crystal Bi based on empirical tight-binding calculations, New J. Phys. **18**, 123015 (2016).

[33] Y. Fuseya and H. Fukuyama, Analytical solutions for the surface states of $Bi_{1-x}Sb_x (0 \leqslant x \lesssim 0.1)$, J. Phys. Soc. Jpn. **87**, 044710 (2018).

[34] T.-R. Chang, Q. Lu, X. Wang, H. Lin, T. Miller, T.-C. Chiang, and G. Bian, Band topology of bismuth quantum films, Crystals **9**, 510 (2019).

[35] I. Aguilera, H.-J. Kim, C. Friedrich, G. Bihlmayer, and S. Blügel, Z_2 topology of bismuth, Phys. Rev. Mater. **5**, L091201 (2021).

[36] C. König, J. C. Greer, and S. Fahy, Effect of strain and many-body corrections on the band inversions and topology of bismuth, Phys. Rev. B **104**, 035127 (2021).

[37] Y. Liu and R. E. Allen, Electronic structure of the semimetals Bi and Sb, Phys. Rev. B **52**, 1566 (1995).

[38] G. Jezequel, J. Thomas, and I. Pollini, Experimental band structure of semimetal bismuth, Phys. Rev. B **56**, 6620 (1997).

[39] T. Hirahara *et al.*, Direct observation of spin splitting in bismuth surface states, Phys. Rev. B **76**, 153305 (2007).

[40] A. Takayama, T. Sato, S. Souma, and T. Takahashi, Giant out-of-plane spin component and the asymmetry of spin polarization in surface Rashba states of bismuth thin film, Phys. Rev. Lett. **106**, 166401 (2011).

[41] I. K. Drozdov, A. Alexandradinata, S. Jeon, S. Nadj-Perge, H. Ji, R. J. Cava, B. Andrei Bernevig, and A. Yazdani, One-dimensional topological edge states of bismuth bilayers, Nat. Phys. **10**, 664 (2014).

[42] F. Schindler *et al.*, Higher-order topology in bismuth, Nat. Phys. **14**, 918 (2018).

[43] T. Shirasawa, M. Ohyama, W. Voegeli, and T. Takahashi, Interface of a Bi(001) film on Si(111)-7 × 7 imaged by surface x-ray diffraction, Phys. Rev. B **84**, 075411 (2011).

[44] M.-Y. Yao, F. Zhu, C. Q. Han, D. D. Guan, C. Liu, D. Qian, and J.-F. Jia, Topologically nontrivial bismuth(111) thin films, Sci. Rep. **6**, 21326 (2016).

[45] H. Ishida, Decay length of surface-state wave functions on Bi (1 1 1), J. Phys. Condens. Matter **29**, 015002 (2016).

[46] G. White, Thermal expansion of trigonal elements at low temperatures: As, Sb and Bi, J. Phys. C **5**, 2731 (1972).

[47] H. Mönig, J. Sun, Y. M. Koroteev, G. Bihlmayer, J. Wells, E. V. Chulkov, K. Pohl, and P. Hofmann, Structure of the (111) surface of bismuth: Leed analysis and first-principles calculations, Phys. Rev. B **72**, 085410 (2005).

[48] E. Tichovolsky and J. Mavroides, Magnetoreflection studies on the band structure of bismuth-antimony alloys, Solid State Commun. **7**, 927 (1969).

[49] M. Vecchi and M. Dresselhaus, Temperature dependence of the band parameters of bismuth, Phys. Rev. B **10**, 771 (1974).

[50] K. Kawaguchi *et al.*, Time-, spin-, and angle-resolved photoemission spectroscopy with a 1-MHz 10.7-eV pulse laser, Rev. Sci. Instrum. **94**, 083902 (2023).

[51] S. D. Ganichev, E. Ivchenko, S. Bel'Kov, S. Tarasenko, M. Sollinger, D. Weiss, W. Wegscheider, and W. Prettl, Spin-galvanic effect, Nature (London) **417**, 153 (2002).

[52] H. Yuan *et al.*, Generation and electric control of spin–valley-coupled circular photogalvanic current in WSe2, Nat. Nanotechnol. **9**, 851 (2014).

[53] M. B. Jungfleisch, Q. Zhang, W. Zhang, J. E. Pearson, R. D. Schaller, H. Wen, and A. Hoffmann, Control of terahertz emission by ultrafast spin-charge current conversion at Rashba interfaces, Phys. Rev. Lett. **120**, 207207 (2018).

[54] C. Zhou *et al.*, Broadband terahertz generation via the interface inverse Rashba-Edelstein effect, Phys. Rev. Lett. **121**, 086801 (2018).

[55] See Supplemental Material at http://link.aps.org/supplemental/10.1103/PhysRevB.110.L041401 for sample preparation; observation of the unoccupied bulk band; electron temperature;

estimation of spin polarization; first-principles calculation; and arguments for the reports that Bi is a HOTI state, which includes Refs. [31,35,41,42,66–79].

[56] Z. Zhao and Y. Kobayashi, Ytterbium fiber-based, 270 fs, 100 W chirped pulse amplification laser system with 1 MHz repetition rate, Appl. Phys. Express **9**, 012701 (2016).

[57] Z. Zhao and Y. Kobayashi, Realization of a mW-level 10.7-eV ($\lambda = 115.6$ nm) laser by cascaded third harmonic generation of a Yb: fiber CPA laser at 1-MHz, Opt. Express **25**, 13517 (2017).

[58] L. Van Hove, The occurrence of singularities in the elastic frequency distribution of a crystal, Phys. Rev. **89**, 1189 (1953).

[59] H. Du *et al.*, Surface Landau levels and spin states in bismuth (111) ultrathin films, Nat. Commun. **7**, 10814 (2016).

[60] K. Yaji, K. Kuroda, S. Toyohisa, A. Harasawa, Y. Ishida, S. Watanabe, C. Chen, K. Kobayashi, F. Komori, and S. Shin, Spin-dependent quantum interference in photoemission process from spin-orbit coupled states, Nat. Commun. **8**, 14588 (2017).

[61] K. Kuroda, K. Yaji, M. Nakayama, A. Harasawa, Y. Ishida, S. Watanabe, C.-T. Chen, T. Kondo, F. Komori, and S. Shin, Coherent control over three-dimensional spin polarization for the spin-orbit coupled surface state of Bi_2Se_3, Phys. Rev. B **94**, 165162 (2016).

[62] R. N. Brown, J. G. Mavroides, and B. Lax, Magnetoreflection in Bismuth, Phys. Rev. **129**, 2055 (1963).

[63] G. E. Smith, G. A. Baraff, and J. M. Rowell, Effective *g* factor of electrons and holes in bismuth, Phys. Rev. **135**, A1118 (1964).

[64] M. Maltz and M. S. Dresselhaus, Magnetoreflection studies in bismuth, Phys. Rev. B **2**, 2877 (1970).

[65] I. Aguilera, C. Friedrich, and S. Blügel, Electronic phase transitions of bismuth under strain from relativistic self-consistent G W calculations, Phys. Rev. B **91**, 125129 (2015).

[66] M. Kammler and M. Horn-von Hoegen, Low energy electron diffraction of epitaxial growth of bismuth on Si(111), Surf. Sci. **576**, 56 (2005).

[67] P. Blaha, K. Schwarz, G. K. H. Madsen, D. Kvasnicka, J. Luitz, R. Laskowski, F. Tran, K. K. Schwarz, and L. D. Marks, WIEN2k, An Augmented Plane Wave + Local Orbitals Program for Calculating Crystal Properties.

[68] P. Blaha, K. Schwarz, F. Tran, R. Laskowski, G. Madsen, and L. Marks, WIEN2k: An APW+lo program for calculating the properties of solids, J. Chem. Phys. **152**, 074101 (2020).

[69] F. Tran and P. Blaha, Accurate band gaps of semiconductors and insulators with a semilocal exchange-correlation potential, Phys. Rev. Lett. **102**, 226401 (2009).

[70] A. D. Becke and E. R. Johnson, A simple effective potential for exchange, J. Chem. Phys. **124**, 221101 (2006).

[71] R. W. G. Wyckoff, Wyckoff, *Crystal Structures*, 2nd ed. (Interscience Publishers, New York, 1963), Vol. 1.

[72] N. Marzari and D. Vanderbilt, Maximally localized generalized Wannier functions for composite energy bands, Phys. Rev. B **56**, 12847 (1997).

[73] I. Souza, N. Marzari, and D. Vanderbilt, Maximally localized Wannier functions for entangled energy bands, Phys. Rev. B **65**, 035109 (2001).

[74] G. Pizzi *et al.*, Wannier90 as a community code: New features and applications, J. Phys.: Condens. Matter **32**, 165902 (2020).

[75] M. P. Lopez Sancho, J. M. Lopez Sancho, J. M. L. Sancho, and J. Rubio, Highly convergent schemes for the calculation of bulk and surface Green functions, J. Phys. F: Met. Phys. **15**, 851 (1985).

[76] L. Aggarwal, P. Zhu, T. L. Hughes, and V. Madhavan, Evidence for higher order topology in Bi and $Bi_{0.92}Sb_{0.08}$, Nat. Commun. **12**, 4420 (2021).

[77] A. Murani *et al.*, Ballistic edge states in Bismuth nanowires revealed by SQUID interferometry, Nat. Commun. **8**, 15941 (2017).

[78] D. Hsieh, D. Qian, L. Wray, Y. Xia, Y. S. Hor, R. J. Cava, and M. Z. Hasan, A topological Dirac insulator in a quantum spin Hall phase, Nature (London) **452**, 970 (2008).

[79] A. K. Nayak, J. Reiner, R. Queiroz, H. Fu, C. Shekhar, B. Yan, C. Felser, N. Avraham, and H. Beidenkopf, Resolving the topological classification of bismuth with topological defects, Sci. Adv. **5**, eaax6996 (2019).